Shot-to-shot 2D IR spectroscopy at 100 kHz using a Yb laser and custom-designed electronics

Farrell, Kieran M ; Ostrander, Josh S ; Jones, Andrew C ; Yakami, Baichhabi R ; Dicke, Sidney S ; Middleton, Chris T ; Hamm, Peter ; Zanni, Martin T

Abstract: The majority of 2D IR spectrometers operate at 1-10 kHz using Ti:Sapphire laser technology. We report a 2D IR spectrometer designed around Yb:KGW laser technology that operates shot-to-shot at 100 kHz. It includes a home-built OPA, a mid-IR pulse shaper, and custom-designed electronics with optional on-chip processing. We report a direct comparison between Yb:KGW and Ti:Sapphire based 2D IR spectrometers. Even though the mid-IR pulse energy is much lower for the Yb:KGW driven system, there is an 8x improvement in signal-to-noise over the 1 kHz Ti:Sapphire driven spectrometer to which it is compared. Experimental data is shown for sub-millimolar concentrations of amides. Advantages and disadvantages of the design are discussed, including thermal background that arises at high repetition rates. This fundamental spectrometer design takes advantage of newly available Yb laser technology in a new way, providing a straightforward means of enhancing sensitivity.

DOI: https://doi.org/10.1364/oe.409360

Originally published at:
Farrell, Kieran M; Ostrander, Josh S; Jones, Andrew C; Yakami, Baichhabi R; Dicke, Sidney S; Middleton, Chris T; Hamm, Peter; Zanni, Martin T (2020). Shot-to-shot 2D IR spectroscopy at 100 kHz using a Yb laser and custom-designed electronics. Optics Express, 28(22):33584.
DOI: https://doi.org/10.1364/oe.409360

Research Article | Vol. 28, No. 22 / 26 October 2020 / Optics Express 33584

Optics EXPRESS

Shot-to-shot 2D IR spectroscopy at 100 kHz using a Yb laser and custom-designed electronics

KIERAN M. FARRELL,[1] JOSH S. OSTRANDER,[1,2] ANDREW C. JONES,[1,3] BAICHHABI R. YAKAMI,[4] SIDNEY S. DICKE,[1] CHRIS T. MIDDLETON,[4] PETER HAMM,[5] AND MARTIN T. ZANNI[1,*]

[1]*Department of Chemistry, University of Wisconsin-Madison, Madison, Wisconsin 53706, USA*
[2]*Currently with the Department of Chemistry, Indiana Wesleyan University, Marion, Indiana 46953, USA*
[3]*Currently with the Center for Integrated Nanotechnologies, Los Alamos National Laboratory, Albuquerque, New Mexico 87185, USA*
[4]*PhaseTech Spectroscopy, 2810 Crossroads Drive, Suite 4000 Madison, Wisconsin 53718, USA*
[5]*Department of Chemistry, University of Zurich, Winterthurerstrasse 190, CH-8057 Zurich, Switzerland*
[*]*zanni@chem.wisc.edu*

Abstract: The majority of 2D IR spectrometers operate at 1-10 kHz using Ti:Sapphire laser technology. We report a 2D IR spectrometer designed around Yb:KGW laser technology that operates shot-to-shot at 100 kHz. It includes a home-built OPA, a mid-IR pulse shaper, and custom-designed electronics with optional on-chip processing. We report a direct comparison between Yb:KGW and Ti:Sapphire based 2D IR spectrometers. Even though the mid-IR pulse energy is much lower for the Yb:KGW driven system, there is an 8x improvement in signal-to-noise over the 1 kHz Ti:Sapphire driven spectrometer to which it is compared. Experimental data is shown for sub-millimolar concentrations of amides. Advantages and disadvantages of the design are discussed, including thermal background that arises at high repetition rates. This fundamental spectrometer design takes advantage of newly available Yb laser technology in a new way, providing a straightforward means of enhancing sensitivity.

1. Introduction

Two-dimensional infrared spectroscopy (2D IR) has proven its utility in answering pertinent questions in diverse fields such as biophysics, materials science, and chemical physics [1,2]. 2D IR spectroscopy can be used to monitor ultrafast phenomena such as chemical exchange and solvent structural dynamics [3–5], as well as slower kinetics such as amyloid aggregation [6–8]. It can be applied to liquids, membranes, and solids [3,9–12], and has recently been implemented in microscopy [13,14], Of course, as true for all techniques, the utility of 2D IR is set by the signal-to-noise ratio (S/N). For 2D IR spectroscopy, the S/N determines the types of vibrational modes that can be used and the concentrations of samples that can be measured, among other properties. This article reports the design and performance of a new 2D IR spectrometer utilizing the high-repetition rate of a Yb:KGW regenerative amplifier.

Commonly used vibrational markers for 2D IR spectroscopy include metal-carbonyls, carbonyls, and amides, because they have large transition dipole strengths [15–18]. Other useful probes include nitriles, azidos, thionitriles, and finger-print stretch modes, but they are more difficult to measure because of their weaker transition dipole strengths [17,19]. Ideally one would use C-D bonds as a site-specific, non-perturbative reporter, but their transition dipole strengths are considerably weak [17,20–23]. Weak absorption can be compensated for by using higher concentrations, so long as the necessary concentrations are attainable and do not affect the structure or dynamics of the analyte. In principle, both strong and weakly absorbing vibrational

#409360 https://doi.org/10.1364/OE.409360
Journal © 2020 Received 4 Sep 2020; revised 8 Oct 2020; accepted 8 Oct 2020; published 22 Oct 2020

Optics EXPRESS

modes can provide large signals at room temperature because their excited vibrational states are effectively unpopulated [24,25]. Thus, the current limitation to 2D IR signal strengths is the laser pulse energy and noise of the spectrometer, not the intrinsic nature of vibrational modes themselves.

To date, the majority of 2D IR spectrometers use Ti:Sapphire regenerative amplifiers that operate at 1-10 kHz repetition rates. In recent years, diode pumped Yb amplifiers have become available that operate at 100 kHz and higher repetition rates. If all else was equal, data collection at 100 kHz would be 100 times faster than at 1 kHz. From a signal-to-noise perspective, a 100 kHz 2D IR spectrometer would have 10-times the S/N of a 1 kHz spectrometer.

However, not all factors are equal. Commercial Ti:Sapphire lasers commonly output 1-10 mJ pulses at a center wavelength of ~800 nm, which can be used to pump an optical parametric amplifier (OPA) and difference frequency generation (DFG) stage to generate 2-30 μJ mid-IR pulses over a range of 3-7 μm. Many Yb amplifiers produce pulses at 1040+/-10 nm with energies ranging from 20-200 μJ at repetition rates of 100 kHz. These ultrafast pulses can pump combined OPA and DFG stages to yield mid-IR pulse energies up to ~2 uJ, although more powerful Yb amplifiers are coming to market. In general, commercial OPA and DFG stages compatible with Yb amplifiers produce a narrower bandwidth than those based on Ti:Sapphire amplifiers. Mid-IR generation requires difference frequency mixing and depends strongly on pump energy and duration, which is why it is not clear whether a high-energy Ti:Sapphire or a lower energy, high repetition rate Yb laser would be superior for 2D IR spectroscopy. These differences were navigated in two prior demonstrations of 2D IR spectroscopy at 100 kHz [26,27]. The 100 kHz 2D IR spectrometer developed by Luther et al. achieved high energy, broad bandwidth mid-IR pulses from an optical parametric chirped pulse amplifier [26]. Donaldson et al. used two Yb:KGW amplifiers to maximize pump energy and probe bandwidth [27,28]. However, it is not immediately clear that a 2D IR spectrometer pumped by a single Yb laser and an OPA will be advantageous compared to existing spectrometers using Ti:Sapphire laser technology.

In this article, we present a new 100 kHz 2D IR spectrometer and compare it to a 1 kHz Ti:Sapphire driven spectrometer. This design features a high energy Yb:KGW amplifier, a home-built OPA, a mid-IR pulse shaper, and custom-designed detection electronics. Electronics were specially tailored for shot-to-shot operation and carefully designed to minimize noise and maximize signal processing speed. Parallel microcontrollers are programmed for flexibility, allowing the user to average data on the chip or read data to the PC shot-to-shot. This laser/spectrometer/electronics design exhibits a 8x enhancement in S/N over a 1 kHz Ti:Sapphire driven spectrometer. S/N is limited by mid-IR power, which can be easily improved by using a commercial OPA. Low concentration benchmark data is reported for amides and nitriles. There is a background signal created in aqueous solvent that appears to be caused by a laser induced temperature rise. The background can be subtracted and more sophisticated methods to mitigate this background are proposed. 2D IR spectrometers designed to take advantage of shot-to-shot data collection at 100 kHz can benefit from their repetition rate, low noise, and long correlation times.

2. Experimental methods

2.1. Mid-infrared light generation

The 1032 nm, 150 μJ, and 270 fs output of a Yb:KGW regenerative amplifier (Pharos, Light Conversion) was converted to the mid-infrared using a home-built two stage OPA and DFG setup. Figure 1 shows a schematic of the two stage OPA based on the design of Mücke *et al.* [29]. The 1032 nm fundamental beam is split along two paths. One path undergoes second harmonic generation (SHG) to produce 516 nm light in a 1 mm type I β barium borate crystal (BBO). The 516 nm light is used to pump the first OPA stage. The other path undergoes white light supercontinuum generation in a yttrium aluminum garnet (YAG) crystal. The white light is

Optics EXPRESS

subsequently stretched and used to seed the first OPA stage. The 516 nm pump and white light seed are collinearly overlapped in a 2.5 mm Type II BBO crystal to yield signal and idler pulses. The temporal overlap of the pump and white light seed was adjusted to tune for the overall output of the OPA. For 5 micron mid-IR after the final DFG interaction, the idler emitted from the first stage should be tuned to 1.7 µm.

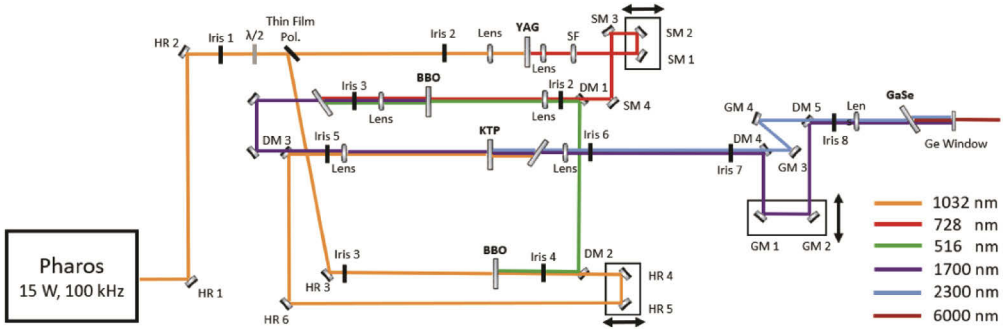

Fig. 1. Schematic and beam diagram for the 100 kHz mid-IR OPA. HR: 1032 nm High Reflector, λ/2: Half Wave plate, SM:Silver mirror, DM: Dichroic mirror, GM: Gold Mirror

Residual 1032 nm fundamental after the SHG process is collinearly overlapped with the 1.7 µm idler in a 5 mm type II potassium titanyl phosphate crystal (KTP) to generate 25 µJ of signal and idler at 1.7 µm and 2.3 µm, respectively. The 1.7 µm signal and 2.3 µm idler are collinearly and temporally overlapped in a 1 mm gallium selenide (GaSe) crystal to produce 5 µm mid-IR light *via* a type II DFG process. The signal and idler wavelengths are chosen to obtain the desired DFG wavelength. The output of the DFG stage was tuned by adjusting the phase matching angle of the GaSe crystal and the signal/idler wavelengths produced by the OPA system to produce the output wavelengths of 4.5-6 µm used in this study. Pumping with 15 W at 100 kHz, the OPA and DFG routinely generated *ca.* 50-90 mW of mid-IR, which corresponds to pulse energies of 0.60-1.00 µJ. According to their specifications, a commercial OPA and DFG from Light Conversion would generate 1.1-2.3 µJ with a 15 W 1032 nm pump.

2.2. 100 kHz 2D IR spectrometer

The 100 kHz 2D IR spectrometer (henceforth referred to as the Yb:KGW spectrometer) itself is very similar to previously published designs [30–32]. It is constructed in the pump-probe geometry using a mid-IR pulse shaper [30,31,33–35]. Mid-IR output from the GaSe is split along pump and probe paths by a 95:5 wedged CaF_2 beam splitter. The pump path is directed into a mid-IR pulse shaper in a horizontal 4f geometry [35]. A pulse shaper uses a diffraction grating to spatially disperse the pump pulse in wavelength and modulate it in amplitude and frequency using a germanium AOM (Isomet Inc.). The first order diffraction from the AOM is subsequently recombined on a second grating to yield a pump pulse pair. Mid-IR pulse shaping grants arbitrary control over pump pulse phases, enabling phase cycling to remove scatter, under sampling, and more [34]. The probe pulse is directed into a retroreflector to control the waiting time delay between the probe and pump pulse pair. When referencing, 50% of the probe beam was split from the probe line prior to the sample for reference detection. Reference detection is only used in the Results section 3.4. Pump and probe beams were focused to an 80 µm spot size using a 90° off-axis parabolic mirror. The probe and reference beams were dispersed by a monochromator (Princeton Instruments) onto each array of a 2×64 pixel MCT array detector (Infrared Associates). However, only 32 elements were used per array, corresponding to a 1×32 or 2×32 array for measurements with and without referencing, respectively. All measurements

Optics EXPRESS

were performed with the *XXXX* polarization scheme [36]. Unless otherwise stated, data was collected by scanning t_1 from 0 to $t_{1,max}$ = 2500 fs, at a t_2 of 0 fs.

2.3. 100 kHz detector amplification and analog-to-digital converter (ADC) electronics

Figure 2 shows a block diagram of the electronic circuit for a measurement card designed to read out 32 pixels of the MCT detector array. Multiple cards are used to read detectors with more pixels, as described below. The elements of the MCT array detector (Infrared Associates) are photo-conductors with a bias current applied *via* R_{Bias}. The amplification OpAmps (½ LT6231 per pixel) feature a very low noise voltage of 1.1nV/√Hz, a high gain-bandwidth product (215 MHz) and a high slew rate (60 V/µs). They are configured as trans-impedance amplifiers with both low and high pass filtering. Their frequency-response (Supplement 1, Fig. S4) has been optimized with two criteria in mind: extract as many charges from the detector elements as possible, while ensuring the signal has decayed to zero after 10 µs (i.e., before the subsequent laser shot) to minimize memory effects from one laser shot to the next. To that end, the time-constant of the high-pass filter, C_1R_{MCT}, was set to 800 ns, which roughly matches the rise time of the MCT signal, and that of the low-pass filter, C_2R_2, to 200 ns. These values were chosen based on simulations that predicted -0.005% of the signal will remain after 10 µs. The experimentally measured ratio is about -0.4%. This discrepancy is attributed to memory intrinsic to the MCT elements. The peak gain has been set to adjust the dynamic range of the MCT detector to that of the ADC (see below).

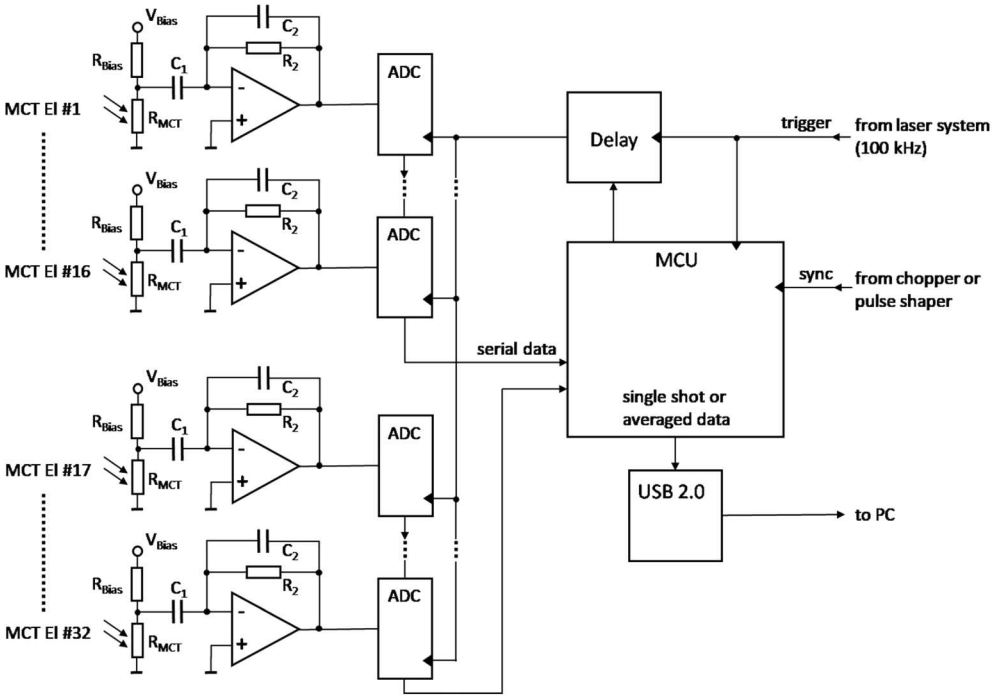

Fig. 2. Block diagram of the electronics designed to read out the MCT detector array at 100 kHz repetition rate; see text for details.

We decided against a switched integrator (such as IVC102) or a sample-and-hold unit to avoid the parasitic capacitances of the switches, which lead to significantly larger memory effects. This decision was made because the high repetition rate of the laser system did not allow for a long enough time to discharge the integration capacitor. Therefore, all signals need to be digitized

Optics EXPRESS

in parallel. While common multi-channel AD conversion cards (e.g., USB-6255, National Instruments) contain only one AD converter that is multiplexed and requires storing of the analog signal, we use a 16 bit ADC converter (½ AD7902 per pixel) triggered from a programmable delay generator (DS1023-500) set to pick the peak of the signal at about 800 ns after the laser pulse. The data are sent to a microcontroller (MCU, STM32F427) by daisy-chaining the ADC converters with 16 channels per serial interface (SPI). The MCU has two SPI's, and thus can handle 32 pixels.

Communication with the PC is performed *via* a USB 2.0 interface, which was chosen because of the ease of its use. Data can be treated in two different ways: The MCU may either send all data "single-shot", in which case data-processing can be performed in the most flexible way. Alternatively, the MCU can average the data on the chip, sorting them into measurement slots synchronized by either a chopper or a pulse shaper. When averaging on the chip, measurement values of all pixels, their squares, as well as the product of each signal pixel and the corresponding reference pixel (for double array detectors) are added up in 4 and 8 byte integers, respectively. This allows one to calculate the mean, standard deviation and cross-correlation between signal and reference pixel. The memory of the MCU can hold 500 such measurement slots, sufficient for measuring a 1650 cm^{-1} vibration (for example) with most phase-cycling schemes in a 1100 cm^{-1} rotating frame. If more measurement slots are needed (up to 1500), one may switch off the calculation of the standard deviation and cross-correlation and calculate only the mean. Averaging-on-the-chip" frees significant amount of computational resources for the PC, and at the same time simplifies data handling significantly. The averaged data are sent to the PC only after a measurement ends, which may contain as many as 65536 laser shots (to avoid overflows) per measurement slot.

If a detector contains more than 32 pixels, measurement cards are cascaded in a synchronized manner; one acting as master and up to three as slaves for a 128 pixel detector. Each measurement card has its own USB 2.0 interface for the communication with the PC. The maximal data rate of USB 2.0 is 60 MB/s, sufficient for a single-shot transfer without any data loss, which amounts to 25 MB/s for a 128 pixel detector. In Supplement 1, Fig. S3 shows a picture of the configuration for a 2×32 pixel detector. The electronics are small enough to be hooked up directly to the detector, avoiding cables for the small signals from the MCT elements to minimize noise-pickup from other electronics in the lab.

Several iterations of the electronics were tested, which differed in their physical layouts and analog amplification scheme. The performance of the most recent and final set of electronics is presented below in Results section 3.2. The 2D IR data was collected using an earlier generation of electronics, but the difference is inconsequential because S/N in the experimental 2D IR data presented below is ultimately limited by fluctuations in probe intensity and not electronic noise for either generation of electronics (Supplement 1, Fig. S5). Alternative to direct detection in the mid-IR, one can upconvert the signal to use a visible wavelength detector [37,38].

2.4. 1 kHz Ti:Sapphire based 2D IR spectrometer for comparison data

1 kHz data used for comparison to the 100 kHz design was collected using a Ti:Sapphire driven spectrometer (henceforth referred to as the Ti:Sapphire spectrometer). A Ti:Sapphire regenerative amplifier (Solstice, Spectra Physics) output 800 nm, 150 mJ and 100 fs pulses at a 1 kHz repetition rate. The output pumped a commercial white-light OPA (Topas-C, Spectra Physics), yielding signal and idler pulses that underwent DFG in $AgGaS_2$ to produce mid-IR pulses. Mid-IR pulse energy was 16.3 μJ for measurements reported here. The design of the 1 kHz spectrometer was identical to the 100 kHz spectrometer described above. The exception being that at 1 kHz, the entire 5.5 cm aperture of the AOM could be used. Pump bandwidth is typically ~130 cm^{-1}. Probe pulses were detected on a 2×64 element MCT array detector (Infrared Associates). Analog

Optics EXPRESS

output of the MCT array was processed using a commercial array integrator (Infrared Systems Development).

2.5. Background subtraction

Solvent background, discussed in section 3.6, was subtracted from low concentration data by collecting a 2D IR spectrum of neat solvent under identical conditions. Solvent subtraction was only performed in this manner for low concentration measurements found in section 3.5 and Supplement 1, Fig. S3. For all other experiments, the background level was inconsequential compared to the foreground. Background from electronic signal introduced by the RFA on the Yb:KGW spectrometer was removed from data in 3.3 by subtracting a 2D IR spectrum collected with the pump pulse blocked.

3. Experimental results

3.1. OPA performance

A chief concern for time-domain nonlinear spectroscopy is pulse energy, duration, and bandwidth. Figure 3(a) shows the spectra of pump and probe pulses tuned to 5 µm. Their FWHM are 132 cm^{-1} and 104 cm^{-1}, respectively. The pump pulse is narrower due to bandwidth losses in the pulse shaper. The pump pulse is compressed using the pulse shaper [34]. To compress, a frequency dependent phase is applied to counteract group velocity dispersion (GVD) and third order dispersion (TOD) introduced by the dispersive optics in the spectrometer. This scheme is implemented by varying the GVD and TOD coefficients, which are the coefficients of the second and third order terms in the Taylor expansion of the spectral phase shown in Eq. (1).

$$\phi_{dc}(\nu) = \frac{1}{2}\beta_{GVD}(\omega - \omega_0)^2 + \frac{1}{6}\beta_{TOD}(\omega - \omega_0)^3 + \ldots \quad (1)$$

Where φ_{dc} is the spectral phase of the pulse, υ_0 is the center frequency of the pulse, and β_{GVD} and β_{TOD} are the GVD and TOD dispersion coefficients, respectively. Phase velocity (zeroth order) and group velocity (first order) terms are omitted, since they do not distort pulse shapes, as were fourth order dispersion (FOD) and higher order terms. In Eq. (1), optimal dispersion compensation is determined empirically by measuring SHG of the mid-IR pulse in an $AgGaS_2$ crystal as a function of the β_{GVD} and β_{TOD} (Fig. 3(b)) A more compressed pulse yields stronger SHG signal. Therefore, we set β_{GVD} and β_{TOD} to the maximum signal in Fig. 3(b).

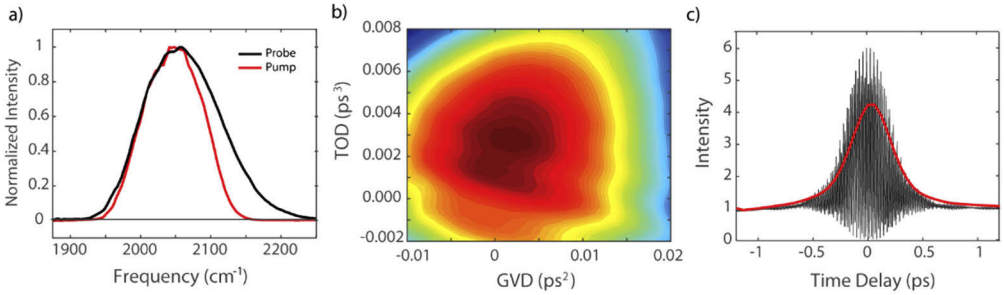

Fig. 3. a) Spectrum of pump and probe pulses centered at 2050cm^{-1} b) GVD and TOD parameter space mapped by scanning second and third order phase coefficients with the pulse shaper c) interferometric (black) and extracted intensity (red) autocorrelation of pump pulse pair after dispersion compensation.

We collected an interferometric autocorrelation of the pump pulse (Fig. 3(c)) by frequency doubling the 5 µm pump with an $AgGaS_2$ crystal and detecting the 2.5 µm second harmonic on

Optics EXPRESS

an InGaAs photodiode. The pulse shaper was used to generate a pair of pulses and scan their relative time delay. To determine the duration of the pulse, the intensity autocorrelation was retrieved by applying a low pass Fourier filter to the interferometric autocorrelation. The FWHM of the extracted intensity autocorrelation in Fig. 3(c) was 459 fs, which corresponds to a 318 fs pump pulse assuming Gaussian pulse shapes. This result is consistent with previously reported 250-300 fs instrument response function obtained from a commercial OPA at 100 kHz [27]. Our pump pulse is over twice the transform limit (141 fs) for a gaussian pulse with 104 cm-1 bandwidth. Improvements might be possible by including higher order dispersion terms when compressing and compensating for angular dispersion of the Bragg angle [39]. It has been shown that active Bragg angle compensation can improve pump pulse duration as much as two-fold [39]. Overall bandwidth might be improved by adding a slight angle between KTP pump and seed beams in the OPA [29]. Mid-IR pulse energies were between 0.60-1.00 μJ. Commercial OPAs can output 1.1-2.3 μJ mid-IR pulses.

3.2. MCT detection electronics performance

Here, we quantify the noise statistics, dynamic range, and linearity of our MCT detector and electronics. To perform our tests, we used a high-power LED (SST-90-R-F11-HG100, Luminos Devices) powered by a laser-diode driver (LDP-V 240-100 V3.3, Picolas). The laser diode driver can produce pulses as short as 50 ns, significantly shorter than the response time of the MCT detector. The LED produces sufficient light to saturate the MCT electronics, despite the visible wavelength (619-623 nm) for which the sensitivity of the MCT detector is poor. The advantage of this setup, in comparison to the output of a mid-IR OPA, is its high stability with a shot-to-shot noise of ≈0.05% and its very uniform illumination of each detector element, due to the incoherent nature of the light source. This light source, rather than the OPA, allows for much more reliable characterization of the intrinsic properties of the MCT detector and the measurement electronics.

Figure 4 shows a measurement of the dark noise, measured with no light hitting the detector, for a 2×32 pixel MCT detector (MCT-32/2-10, Infrared Associates) with element sizes of 0.5×1 mm^2, a dark resistance of ≈100 Ω and a bias current of 10 mA. The standard deviation of the shot-to-shot fluctuations is ~6 counts (inset, in blue), out of the 65535 counts of the 16 bit ADC. Furthermore, the noise is perfectly δ-correlated (main panel, in red), indicating that there is no pick-up from any high-frequency signals in the measurement electronics. When replacing an MCT detector element with a conventional resistor with the same resistance, the noise goes down to ~3 counts, which is the thermal noise of that resistor. Therefore, we conclude that the noise of the overall setup is not limited by the measurement electronics but is intrinsic to the MCT detector.

Figure 5 plots the linearity of the MCT detector. It has been measured by inserting a 1% neutral density (ND) filter in a flip mount and a continuous ND filter wheel into the beam path. The continuous ND filter was used to vary the light intensity on the detector. The 1% ND filter, in turn, gave the reading for the abscissa of the plot in Fig. 5 when flipped into the beam path, and that of the ordinate when flipped out. Assuming that the detector is in a linear regime when the 1% ND filter is inserted, the measurement reveals the linearity of the detector. The red line in Fig. 5 shows a fit of the data by a 2nd-order polynomial, and the black line the linear part of that fit function. As common for MCT detectors, the response deviates from linearity rather early but enters saturation only very slowly. At the maximum counts of the 16 bit ADC, the response deviates by -10% from linear, which we consider the upper limit for viable data collection. Linearity is important, because non-linearity causes artifacts in Fourier transform spectroscopies [40–43]. We use -10% deviation from linearity for the definition of the dynamic range of the MCT detector, although signals can be computationally scaled to reduce the deviation, which we do not do here. The overall gain of the input amplifier (Supplement 1, Fig. S4) has been adjusted with that criterion in mind. Together with the noise of 6 counts shown in Fig. 4, the dynamic

Optics EXPRESS

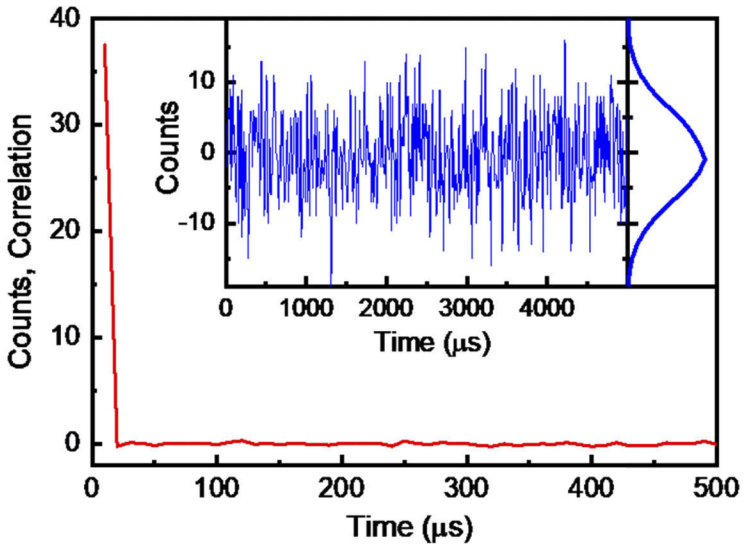

Fig. 4. Dark noise of measurement electronics and MCT detector. The inset (blue) shows measurement values over 500 laser shots (5 ms) together with a distribution function (right), revealing a standard deviation of ≈6 counts. The main panel (red) shows an auto-correlation function of the noise.

range of the detector and electronics is 65535/6≈10000. That number limits the detectivity to 40 µOD for a single laser shot. One has to keep in mind, though, that this high dynamic range will be reached only if homogeneously illuminating the complete MCT detector elements.

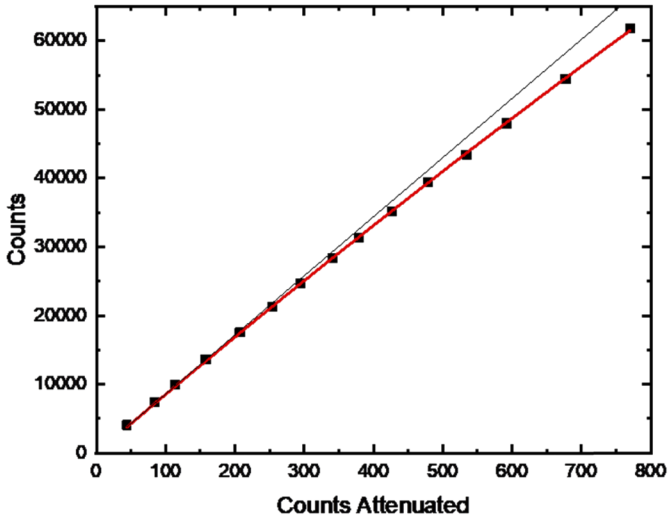

Fig. 5. Linearity of the MCT detector measured with 50 ns pulses from a red LED (see text for details). The data (black squares) are fit by a 2nd-order polynomial (red line), while the linear part of that fit is shown as a thin black line.

Optics EXPRESS

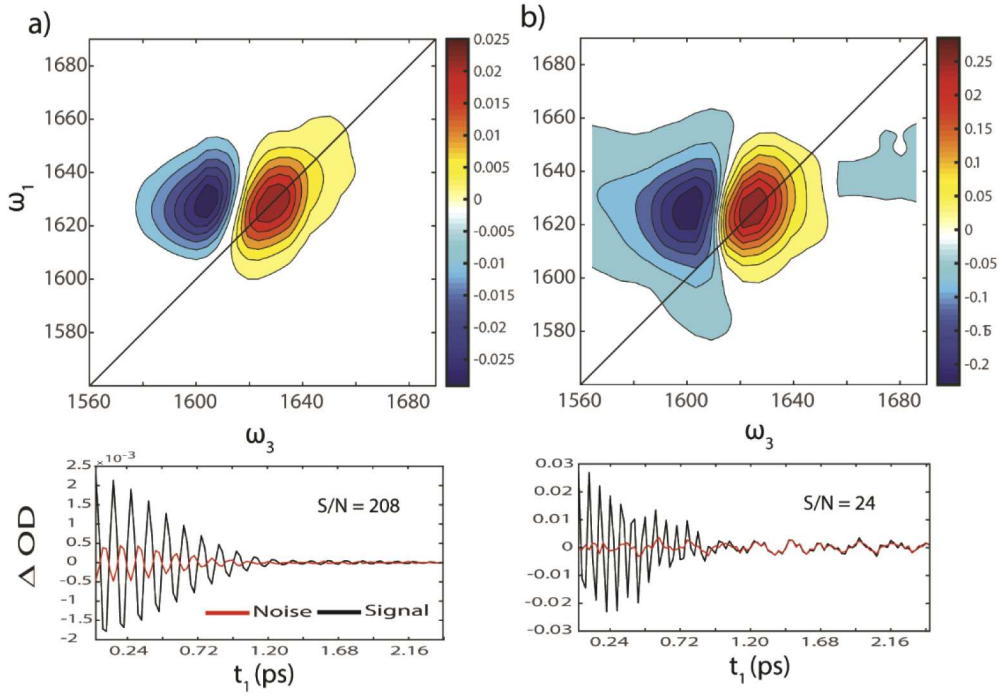

Fig. 6. Sample of 100 mM NMA collected on a a) Yb:KGW spectrometer and a b) Ti:Sapphire spectrometer. Spectra were averaged for 10 minutes each. Lower panel show time domain data used to calculate S/N.

3.3. *Signal-to-noise ratio determination*

In this section, we compare the S/N of the 100 kHz Yb:KGW spectrometer to a 1 kHz Ti:Sapphire 2D IR spectrometer. Figure 6 shows the spectrum of 100 mM n-methylacetamide (NMA) in D_2O collected on 100 kHz Yb:KGW and 1 kHz Ti:Sapphire spectrometers with 10 minutes of averaging. At 6 µm excitation, each spectrometer loses 35-40% pulse energy between the OPA output and the sample, largely due to water vapor absorption. Pulse shaper efficiencies on each spectrometer were 25-30%. Sample cells consisted of two 2 mm CaF_2 windows separated by a 50 µm spacer (5.6 mm optical path length). The element dimensions for the arrays used on the Yb:KGW and Ti:Sapphire spectrometers were 1×0.2 mm and 1×0.25 mm, respectively. This difference should be inconsequential to the comparison because the noise was limited by probe intensity fluctuations and not detector noise. The amplitude of the spectrum collected with the Yb:KGW spectrometer is 1/10 that of the Ti:Sapphire spectrometer. The S/N was calculated in the time domain. We estimate the S/N in the time-domain because the comparison is straightforward, whereas in the frequency domain the noise is not uniformly distributed, making it more difficult to quantitatively compare. We used different rotating frames in the two experiments (Figs. 6(a) and 6(b), respectively). Because we computed the S/N in the time-domain, the choice of rotating frame does not impact the analysis. Traces of time domain data were examined at a probe pixel where there was no signal at the end of the free induction decay and a probe pixel where there was maximum bleach signal. S/N was calculated as the ratio between the maximum of the bleach trace at early t_1 times and the average intensity of the noise trace at longer t_1 times. Measured this way, the NMA spectrum recorded at 100 kHz had a S/N of 208, whereas the spectrum recorded at 1 kHz had a S/N of 24. Thus, the 100 kHz Yb:KGW spectrometer has a 8x improvement in S/N.

Optics EXPRESS

The 8x improvement in S/N largely occurs because the noise of the Yb laser is much lower than that of the Ti:Sapphire. Figure 7 shows change in signal (ΔOD) from an off-diagonal point on the 2D spectrum as a function of averaging time for the 100 kHz Yb:KGW system and the 1 kHz Ti:Sapphire system. Measured this way, the noise on the Yb:KGW spectrometer is two orders of magnitude lower than the Ti:Sapphire spectrometer (See Fig. 7). For the both systems, off-diagonal noise decreased rapidly within 10 minutes of averaging, after which S/N slowly improves through 30 minutes. From the point on, S/N does not appear to improve. It is not clear why the noise does not continue to improve, but we suspect that it is due to low-frequency noise from air current and thermal drifts, although these effects have not been investigated. Thus, while the signal strength on the Yb:KGW spectrometer is smaller due to lower pulse power, the higher repetition rate and lower noise of the Yb:KGW results in the the 8x improvement in S/N.

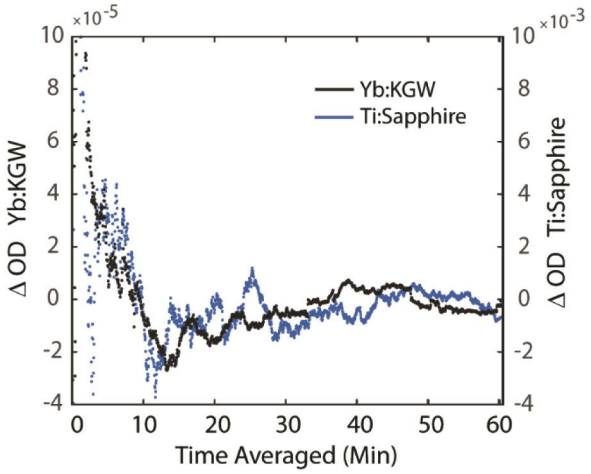

Fig. 7. Change in signal decrease over one hour of averaging. 2D IR intensity obtained from a representative off-diagonal datapoint from Yb:KGW (ν_{pu}=1670 cm^{-1}, ν_{pr}=1631 cm^{-1}) and Ti:Sapphire (ν_{pu}=1686 cm^{-1}, ν_{pr}=1624 cm^{-1}) spectrometer spectra in Fig. 6(a) and Fig. 6(b).

We note that the S/N enhancement is different when calculated in the frequency domain and that it depends on the choice of rotating frame. When calculating S/N in the frequency domain, data in Fig. 6 corresponds to a 4-5x improvement. It is also important to note that we are comparing data collected with 2D IR spectrometers that each use mid-IR pulse shaping. Using pulse shaping, the delays and phases between the pump pulses are updated shot-to-shot in each spectrometer [31,32,34]. Because choppers and delay stages cannot operate instantaneously, the contrast in S/N between a 100 kHz spectrometer operating with a pulse shaper to an analogous 1 kHz spectrometer using conventional optics would be much starker. Indeed, the comparison was made at 100 kHz for a 2D-Visible spectrometer, which showed that shot-to-shot scanning gives an additional 30x improvement in S/N [44].

Lastly, we note that the enhancement provided by this spectrometer is not a general result. The noise statistics are largely determined by the stability of the regenerative amplifier. Different amplifiers may exhibit different noise statistics. For example, commercial OPAs for Yb lasers specify roughly twice the pulse energy of our homebuilt system and there exist much higher powered 1kHz Ti:Sapphire amplifiers than the used here. The long term stability is another advantage of Yb lasers not considered here. In Supplement 1, Fig. S5 shows the power spectral density of the mid-IR probe from the Yb:KGW/OPA source reported here. Furthermore, this S/N

Optics EXPRESS

enhancement can be further improved by increasing mid-IR pulse energy using a commercial OPA or OPCPA source.

3.4. Methods of improving S/N

All data above was collected without using the reference beam (see Experimental). As Supplement 1, Fig. S5 shows, instrument noise was limited by fluctuations in probe intensity rather than detector noise. Noise from probe intensity fluctuations can be removed by referencing. In this section, we implement a referencing method introduced by Feng *et. al.* that corrects for signal/reference array mismatch using a correlation matrix [45,46]. Robben et *al.* have explored a variation of correlation matrix referencing that uses edge pixels on the signal array in lieu of a separate reference array [47]. We introduce a simple computational method for background subtraction that we call "spectral baseline removal". Experimental details about how we evaluated the correlation matrix and implemented this referencing method are outlined in the SI.

Figures 8(a)-(c) shows the spectra of 100 µM NaN_3 in D_2O collected in 41 seconds without referencing, with correlation matrix referencing, and with spectral baseline removal. A 4x increase in S/N was calculated for correlation matrix referencing relative to no referencing. Referencing efficiently reduced noise from local oscillator fluctuations; however, the spectrum in Fig. 8(b) shows that the 2D IR signal rests upon a negative baseline. We attribute baseline depression to pump induced background, which cannot be removed by referencing. In the time domain, this background can be seen at early t_1 delays and varies slowly across the probe axis. It is out of phase with the bleach and in phase with the overtone, causing unequal bleach and overtone amplitudes.

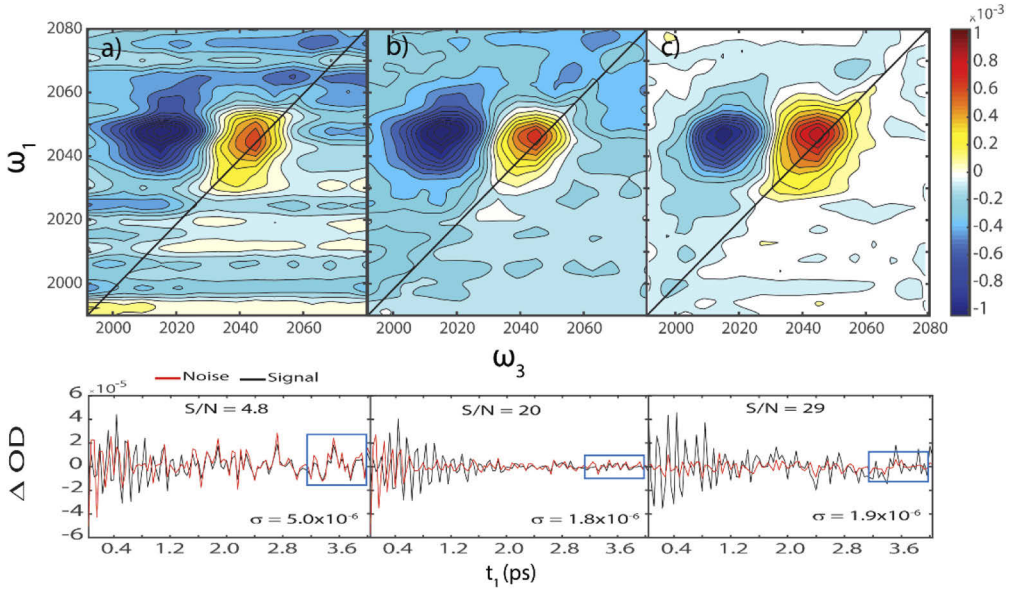

Fig. 8. 2D IR spectra of 100 µM sodium azide obtained a) without referencing, b) with referencing using a correlation matrix estimated from 8,000 pump off shots before data collection, and c) with a gaussian fit background correction. Blue boxes in lower panels show region over which the standard deviation of the noise trace was evaluated.

We introduce an alternative method for reducing noise from local oscillator fluctuations that we refer to as spectral baseline removal. Details on how to implement the technique and avoid artifacts are discussed at length in the SI. To track shot-to-shot local oscillator fluctuations, probe spectra used to calculate a 2D IR spectrum are fit by a Gaussian or a polynomial. The

Optics EXPRESS

polynomial is then subtracted from the experimental data. Figure 8(c) shows the same 100 µM NaN_3 spectrum after applying spectral baseline removal instead of referencing. Spectral baseline removal resulted in a 6x improvement in S/N over the spectrum in Fig. 9(a). Like referencing, background fitting efficiently reduced noise from local oscillator fluctuations. Importantly, by comparing the noise traces in Figs. 8(b) and 8(c) at early t_1 delays, it is clear that spectral baseline removal also reduces the pump induced background, as seen in Fig. 8(c) in which the baseline of the 2D spectrum is no longer negative and the fundamental and overtone transitions have similar amplitudes. For the remainder of this manuscript, we apply a polynomial fit of background truncated at first order.

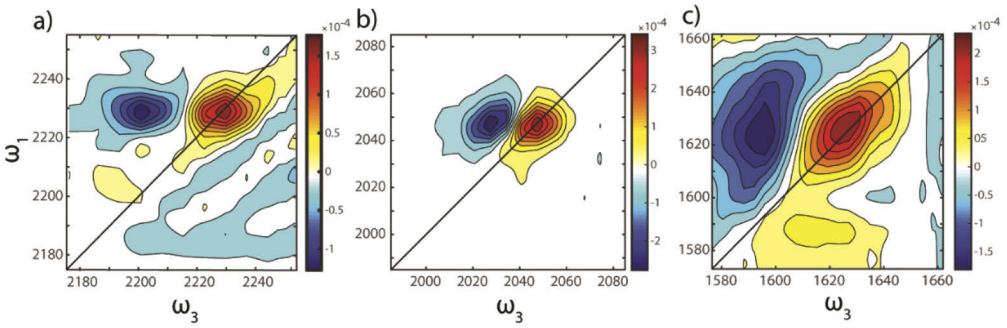

Fig. 9. 2D IR spectra of (a) 1 mM CNPh, (b) 10 µM ReCO, and (c) 500 µM NMA. All spectra were averaged for 820 seconds. The CNPh spectrum was collected at a waiting time of 1 ps to mitigate solvent background at 4.5 µm excitation. Data in panels a and b were collected with $t_{1,max}$=4 ps.

3.5. *Low concentration measurements*

We tested the performance of the 100 kHz 2D IR spectrometer on a series of samples. Figure 9 reports the spectra and concentration of 4-cyanophenol (CNPh), rhenium pentachlorocarbonyl (ReCO), and NMA at 1 mM, 10 µM, and 500 µM, respectively. All spectra were recorded in 820 seconds. CNPh was chosen because it is identical to the side chain of *p*-cyano-phenylalanine, an unnatural amino acid that has been used to probe structure and solvation of proteins and protein inhibitors [48–50]. Nitrile probes are often used for 2D IR experiments at concentrations of >5 mM [48,51–53]. ReCO was chosen because metal carbonyls are often used as model systems in 2D IR spectroscopy. With sufficient averaging, it is possible to measure a single monolayer of metal-carbonyls [54,55].

NMA is representative of a peptide monomer because it has an amide I vibration [56]. With 820 s of averaging, the lowest attainable concentration was 500 µM. NMA's transition dipole strength is near that of a random coil peptide configuration [57–59]. Thus, polypeptide and proteins should be measurable at even lower concentrations; Supplement 1, Fig. S6 shows a 2D IR spectrum collected at 150 µM after 10 seconds of averaging for the 37 amino acid hIAPP polypeptide. The signal strength of 2D IR spectroscopy scales quadratically with the transition dipole strength. α-helices and β-sheets have transition dipoles strengths 2-5 times larger than a random coil, and thus should be measurable at very small concentrations [59–61].

Enhanced S/N improves measurement of kinetics, such as aggregation of amyloid proteins, using a technique we call "rapid-scan" 2D IR spectroscopy [32,34]. These experiments are not photo-triggered like in "transient" 2D IR spectroscopy. Rather, kinetics experiments are carried out by irreversibly initiating a process (e.g. by dissolving a protein) and continuously scanning 2D IR spectra. A running average is then performed to obtain sufficient S/N. Thus, the S/N sets the time resolution. In Supplement 1, Fig. S6 shows that the 100 kHz 2D IR spectrometer can

Optics EXPRESS

measure spectra of random coil and fibrillar 150 µM hIAPP with a running average using a 10 second window. Thus, early conformational changes in aggregation kinetics can be monitored. Tracy *et al.* have shown that 100 kHz 2D IR is useful for investigating fast chemical kinetics *via* a microfluidic solvent mixing approach [62].

We note, as written in the Experimental, that a solvent background signal was subtracted from these spectra. The origins of this solvent background are discussed in section 3.6.

3.6. Observation of temperature induced transient grating background

We have also observed an artifact along the diagonal of the 2D IR spectra that we propose is induced by accumulated thermal gratings. Figure 10(a) shows a spectrum of neat D_2O which has a sharp feature along the diagonal. This feature did not decrease with averaging. Its intensity scales with the thickness of the sample and pulse energy. The response of the artifact to pulse polarization is consistent with a molecular response [36]. In the time-domain, the artifact decays slowly with t_1 (still present at t_1=4 ps), but rapidly (~1 ps lifetime) over t_2. It is not present in chloroform and other solvents that have little-to-no absorption in this wavelength range. Its anti-diagonal width is set by the maximum t_1 delay and becomes extremely narrow for large t_1. The artifact in Fig. 10 is ~5 cm^{-1} wide because $t_{1,max}$ was set at 4 ps, which is narrower than the antidiagonal linewidth of most molecules. Finally, the sign of the signal depends on the phases of pulses from different laser shots. Artifacts can be caused by the pulse shaper or detector if either is operated near saturation [63], which was not the case as data was collected within the linear regime of the pulse shaper and detector. From these observations, we conclude that the feature is caused by a temperature induced memory effect, which we confirm with the simulations given below.

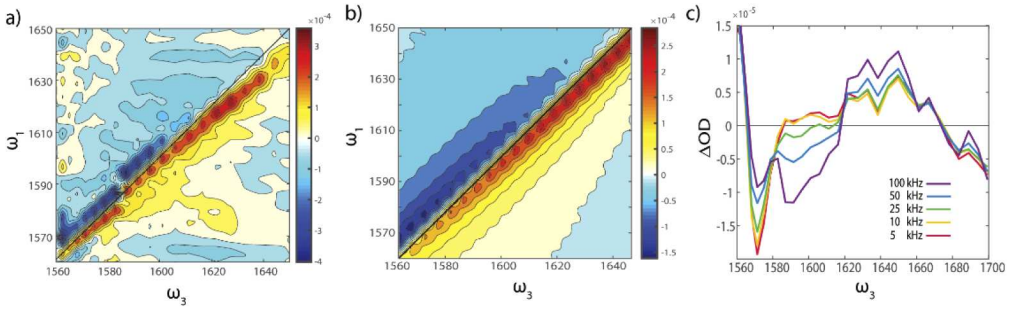

Fig. 10. a) Solvent background artifact observed in neat D_2O with 6 µm excitation measured with $t_{1,max}$ = 4 ps, b) Simulation of solvent background according to the proposed transient grating mechanism. c) Transient absorption spectrum at reduced repetition rates. Transient absorption spectra were obtained from a separate pump-probe measurement with t_2 = 0 fs.

Perhaps the strongest pieces of evidence for the origin of the artifact is that its intensity also depends on the laser repetition rate. Figure 10(c) shows the transient absorption spectrum of neat D_2O collected at repetition rates from 5 to 100 kHz. The artifact decreases systematically with repetition rate and is difficult to resolve at 10 kHz or less.

Photon energy absorbed by the sample excites vibrational modes that ultimately relax, thermalizing the solvent and causing a temperature increase (i.e. a T-jump). If that excess heat does not diffuse from the laser spot before the next laser shot, then the T-jump will affect the data collected by the next laser shot. Sample heating can affect the measurements in three different ways. First, low frequency modes gain population, which creates new combination bands to the modes of interest, broadening the spectrum. Donaldson *et. al* evaluated this effect in their 100 kHz 2D IR spectrometer by comparing the peak frequencies between an FTIR spectrum at an

Optics EXPRESS

elevated temperature to the v = 0-1 transition in their spectrometer [27]. They concluded that this effect is negligible in D_2O at 6 μm excitation. Second, a thermal lens can alter the focus of the laser beams, which typically decreases 2D IR signal. The above effects distort lineshapes and intensities of 2D IR signal, but does not explain the artifacts in Fig. 10(a). Third, a thermal grating is created that affects measurements made by subsequent shots. Some thermal gratings will have an intensity that depends on the relative time-delay and phases applied with the pulse shaper. Because the grating intensity depends on the relative time delay, signals created by the grating survive the Fourier transform, thereby introducing an artifact to the 2D IR spectrum.

The 2D IR pulse sequence in our experiments consists of two collinear pump pulses and a probe pulse denoted E_1, E_2, and E_3, respectively. E_1 and E_2 are separated by t_1 and E_2 and E_3 are separated by t_2. The pump pulses are each programmed with an arbitrary phase, φ_1 and φ_2, respectively, while φ_3 is the phase of the probe pulse. The delays and phases are varied shot-to-shot according to the phase cycling scheme being used [30,34]. For each laser shot, a coherent thermal grating will be created between all pair-wise combinations of pulses, i.e. E_1/E_2, E_1/E_3, and E_2/E_3. The incoherent thermal gratings (E_1/E_1 etc.) created by each pulse are removed by the phase cycling and are therefore ignored.

The observed artifact is best explained as a photon echo stimulated by a pulse (either E1, E2, or E3) from a thermal grating excited by pulses from a prior laser shot. An analogous event was first observed at 1 kHz by Schanz *et al.* [64]. In this scenario, such a process generates a variety of Feynman pathways, four of which survive the rotating wave approximation, phase matching, and phase cycling. The three Feynman pathways plausibly responsible for diagonal artifact in Fig. 10(a) are shown in Fig. 11. Signals arising from pathways with different phase matching directions are observed experimentally in the presence of scatter. The pathway shown in Fig. 11(b) is the most dominant contribution to the diagonal background because the grating does not decay by the homogeneous linewidth over t_1. The equation for this pathway (Fig. 11(b)) excited by a pulse n shots prior is shown in Eq. (2) is compared to a typical rephasing 2D IR pathway in Eq. (3).

$$S^{n}_{grating} \propto i\widetilde{E}_2\widetilde{E}_3\widetilde{E}_1\mu_{01}^4 \exp[-i(\varphi_1^N - \varphi_2^{N-n})] \exp(-i\omega t_2) \exp[i\omega(t_1 + t_3)] \exp[-\Gamma_1(t_2 + t_3)] \exp[-\Gamma_T(n \times 10\mu s - t_1 - t_2)] \tag{2}$$

$$S^{n}_{2DIR} \propto i\widetilde{E}_2\widetilde{E}_3\widetilde{E}_1\mu_{01}^4 \exp[-i(\varphi_1^N - \varphi_2^{N-n})] \exp(-i\omega t_1) \exp(i\omega t_3) \exp[-\Gamma_1(t_1 + t_3)] \exp(-\Gamma_2 t_2) \tag{3}$$

In Eqs. (2) and (3), N represents the current shot, whereas n represents the number of shots prior. Γ_1 and Γ_2 are the dephasing time and population lifetime, respectively. Γ_T is the thermal relaxation of the solvent. The 2D IR signal depends on the relative phase between pump pulses of a single laser shot, whereas the thermal grating signal depends on the relative phase between pump pulses of different laser shots, consistent with experimental observations.

We simulated the signal stimulated from accumulated thermal gratings. To estimate Γ_T, we solved the diffusion equation numerically for an 80 μm focal spot size and a 50 μm spacer [65]. The result is a stretched exponential that extends over several milliseconds. Since each laser shot is spaced by 10 μs, multiple thermal gratings will contribute. The observed thermal grating signal is given by the sum in Eq. (4). In Eq. (4), the thermal decay is represented as an exponential decay with lifetime Γ_T for simplicity, although in reality it has stretched exponential form. The simulated thermal response is shown in Fig. 10(b), which closely resembles the experiment in Fig. 10(a). As observed in experiment, the simulated signal also becomes narrower with

Optics EXPRESS

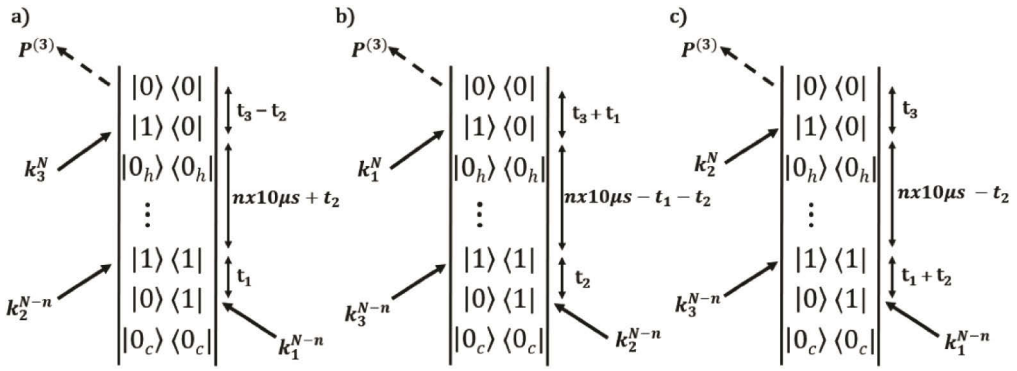

Fig. 11. Feynman pathways responsible for diagonal artifact shown in Fig. 10(a). A pulse from laser shot N stimulates an echo from a coherent population grating excited by pulses from n laser shots prior. The subscript *h* indicates a ground state thermal population grating (h for "hot"). The subscript *c* indicates a ground state at room temperature (c for "cold").

increased $t_{1,max}$ and matches the measured phase dependence.

$$S^n_{grating} \propto i\widetilde{E}_2\widetilde{E}_3\widetilde{E}_1\mu_{01}^4 \sum_{n=1}^{N} \left\{ \begin{array}{l} \exp[-i(\varphi_1^N - \varphi_2^{N-n})]\exp(-i\omega t_2)\exp[i\omega(t_1+t_3)]\ldots \\ \ldots\exp[-\Gamma_1(t_1+t_3)]\exp[-\Gamma_T(n\times 10\mu s - t_1 - t_2)] \end{array} \right\} \quad (4)$$

The phase dependence of the accumulated thermal grating is not analytically identical to 2D IR signal, as can be seen by comparing Eqs. (2) and (3). Thus, it should be possible to remove the accumulated grating artifact using a new phase cycling scheme that is a function of the laser shot. It should also be possible to differentiate and subtract the thermal background by scanning t_1 to delays where the artifact has a much narrower linewidth than the molecular signal. Of course, flowing the sample or raster scanning the laser pulses to refresh the sample shot-to-shot would also decrease or remove the thermal grating. We do not pursue these steps here because the S/N of this Yb spectrometer already exceeds the Ti:Sapphire to which it is compared.

4. Conclusions and outlook

We demonstrate that a 100 kHz 2D IR spectrometer outputting only ~1 uJ of mid-IR light using a single Yb:KGW amplifier and OPA improves the S/N by 8-times over 1 kHz Ti:Sapphire/OPA spectrometer outputting 16.3 uJ of mid-IR. We provided detailed blueprints for the two-stage OPA and rapid readout MCT detection electronics. Our OPA and DFG system was shown to produce pulses broad enough in bandwidth to sample the amide I vibration and short enough in duration for mid-IR investigations. A new design for electronic readout of the MCT was presented. Detector noise and linearity was found to be limited by the MCT array rather than electronics themselves, providing optimal dynamic range.

Our analysis shows that for 6 µm excitation, this 100 kHz spectrometer/amplifier system shows an 8x enhancement over the 1 kHz spectrometer to which is was compared. Referencing using a correlation matrix was shown to further improve this enhancement four-fold. An alternative to referencing, referred to as shot-to-shot background subtraction, was shown to improve S/N 6x and reduce pump-induced thermal backgrounds. We found that thermal effects at 100 kHz are not negligible and generate scatter-like artifacts. These artifacts can be subtracted using a solvent background scan and we discussed methods for reducing this effect.

The high stability and low cost of high repetition rate Yb lasers are having a dramatic impact on the ultrafast sciences. To take full advantage of high repetition rates, one wants to scan

Optics EXPRESS

delays and phase cycle shot-to-shot. Pulse shaping with a transverse acousto optic modulator can be used at 100 kHz and higher repetition rates. The MCT detection electronics reported here allow the user to take advantage of shot-to-shot readout up to 100 kHz. We home-built our OPA, but commercial OPAs and OPCPAs provide 2-3x the pulse energy; therefore, incorporating these sources could provide 4-9x faster spectral acquisition than reported here. We compared a Light Conversion Yb laser to a Spectra Physics Ti:Sapphire system only because those are the lasers available to us. Spectra Physics also manufactures Yb lasers. We recently reported a spectrometer for collecting 2D White-Light (broadband visible) Spectroscopy at 100 kHz using a Spectra Physics Yb:KYW amplifier whose performance far exceeded a Ti:Sapphire pumped spectrometer [41]. As noted in the Introduction, the eigenstate energies of vibrational modes far exceed thermal fluctuations and so we anticipate that future technical advances will continue to improve the sensitivity of 2D IR spectroscopy.

Funding

National Institutes of Health (R01DK079895, R01GM102387); National Science Foundation (DGE-1747503); Office of the Vice Chancellor for Research and Graduate Education, University of Wisconsin-Madison; Wisconsin Alumni Research Foundation.

Acknowledgements

Support for this research was provided by the Office of the Vice Chancellor for Research and Graduate Education at the University of Wisconsin–Madison with funding from the Wisconsin Alumni Research Foundation. K.M.F is grateful for funding from the National Science Foundation Graduate Research Fellowship Program under Grant No. DGE-1747503. Funding also came from the NIH via grants NIDDK R01DK079895. Any opinions, findings, and conclusions or recommendations expressed in this material are those of the authors and do not necessarily reflect the views of the National Science Foundation.

Disclosures

The authors declare the following competing financial interest(s): M.T.Z. and C.T.M are co-owners of PhaseTech Spectroscopy, Inc., which sells 2D IR/visible spectrometers, pulse shapers, and high-repetition rate MCT detection electronics (I,E,P). B.R.Y is an employee of PhaseTech Spectroscopy (P).

See Supplement 1 for supporting content.

References

1. M. K. Petti, J. P. Lomont, M. Maj, and M. T. Zanni, "Two-dimensional spectroscopy Is being used to address core scientific questions in biology and materials science," J. Phys. Chem. B **122**(6), 1771–1780 (2018).
2. N. T. Hunt, "2D-IR spectroscopy: ultrafast insights into biomolecule structure and function," Chem. Soc. Rev. **38**(7), 1837–1848 (2009).
3. M. D. Fayer, "Dynamics of liquids, molecules, and proteins measured with ultrafast 2D IR vibrational echo chemical exchange spectroscopy," Annu. Rev. Phys. Chem. **60**(1), 21–38 (2009).
4. S. T. Roberts, K. Ramasesha, and A. Tokmakoff, "Structural rearrangements in water viewed through two-dimensional infrared spectroscopy," Acc. Chem. Res. **42**(9), 1239–1249 (2009).
5. M. Khalil, N. Demirdöven, and A. Tokmakoff, "Coherent 2D IR spectroscopy: molecular structure and dynamics in solution," J. Phys. Chem. A **107**(27), 5258–5279 (2003).
6. L. E. Buchanan, E. B. Dunkelberger, H. Q. Tran, P. N. Cheng, C. C. Chiu, P. Cao, D. P. Raleigh, J. J. De Pablo, J. S. Nowick, and M. T. Zanni, "Mechanism of IAPP amyloid fibril formation involves an intermediate with a transient β-sheet," Proc. Natl. Acad. Sci. U. S. A. **110**(48), 19285–19290 (2013).

Optics EXPRESS

7. A. L. Serrano, J. P. Lomont, L. Tu, D. P. Raleigh, and M. T. Zanni, "A free energy barrier caused by the refolding of an oligomeric intermediate controls the lag time of amyloid formation by hIAPP," J. Am. Chem. Soc. **139**(46), 16748–16758 (2017).
8. A. Abedini, A. Plesner, P. Cao, Z. Ridgway, J. Zhang, L. H. Tu, C. T. Middleton, B. Chao, D. J. Sartori, F. Meng, H. Wang, A. Wong, M. T. Zanni, C. B. Verchere, D. P. Raleigh, and A. M. Schmidt, "Time-resolved studies define the nature of toxic IAPP intermediates, providing insight for anti-amyloidosis therapeutics," eLife **5**, 12977 (2016).
9. H. T. Kratochvil, M. Maj, K. Matulef, A. W. Annen, J. Ostmeyer, E. Perozo, B. Roux, F. I. Valiyaveetil, and M. T. Zanni, "Probing the effects of gating on the ion occupancy of the K+ channel selectivity filter using two-dimensional infrared spectroscopy," J. Am. Chem. Soc. **139**(26), 8837–8845 (2017).
10. H. T. Kratochvil, J. K. Carr, K. Matulef, A. W. Annen, H. Li, M. Maj, J. Ostmeyer, A. L. Serrano, H. Raghuraman, S. D. Moran, J. L. Skinner, E. Perozo, B. Roux, F. I. Valiyaveetil, and M. T. Zanni, "Instantaneous ion configurations in the K+ ion channel selectivity filter revealed by 2D IR spectroscopy," Science **353**(6303), 1040–1044 (2016).
11. J. J. Hermans, L. Baij, M. Koenis, K. Keune, P. D. Iedema, and S. Woutersen, "2D-IR spectroscopy for oil paint conservation: elucidating the water-sensitive structure of zinc carboxylate clusters in ionomers," Sci. Adv. **5**(6), eaaw3592 (2019).
12. A. A. Eigner, T. C. Anglin, and A. M. Massari, "2D-IR studies of annealing-induced changes to structural dynamics in organic semiconductor thin films," J. Phys. Chem. C **114**(28), 12308–12315 (2010).
13. J. S. Ostrander, A. L. Serrano, A. Ghosh, and M. T. Zanni, "Spatially resolved two-dimensional infrared spectroscopy via wide-field microscopy," ACS Photonics **3**(7), 1315–1323 (2016).
14. C. R. Baiz, D. Schach, and A. Tokmakoff, "Ultrafast 2D IR microscopy," Opt. Express **22**(15), 18724–18735 (2014).
15. A. M. Woys, S. S. Mukherjee, D. R. Skoff, S. D. Moran, and M. T. Zanni, "A strongly absorbing class of non-natural labels for probing protein electrostatics and solvation with FTIR and 2D IR spectroscopies," J. Phys. Chem. B **117**(17), 5009–5018 (2013).
16. S. D. Fried, S. Bagchi, and S. G. Boxer, "Measuring electrostatic fields in both hydrogen-bonding and non-hydrogen-bonding environments using carbonyl vibrational probes," J. Am. Chem. Soc. **135**(30), 11181–11192 (2013).
17. J. Ma, I. M. Pazos, W. Zhang, R. M. Culik, and F. Gai, "Site-specific infrared probes," Annu. Rev. Phys. Chem. **66**(1), 357–377 (2015).
18. M. J. Tucker, X. S. Gai, E. F. Fenlon, S. H. Brewer, and R. M. Hochstrasser, "2D IR photon echo of azido-probes for biomolecular dynamics," Phys. Chem. Chem. Phys. **13**(6), 2237–2241 (2011).
19. Z. Getahun, C. Huang, T. Wang, B. De León, W. F. DeGrado, and F. Gai, "Using nitrile-derivatized amino acids as infrared probes of local environment," J. Am. Chem. Soc. **125**(2), 405–411 (2003).
20. M. W. Nydegger, W. Rock, and C. M. Cheatum, "2D IR spectroscopy of the C – D stretching vibration of the deuterated formic acid dimer," Phys. Chem. Chem. Phys. **13**(13), 6098–6104 (2011).
21. K. Gündoğdu, M. W. Nydegger, J. N. Bandaria, S. E. Hill, and C. M. Cheatum, "Vibrational relaxation of C-D stretching vibrations in $CDCl_3$, $CDBr_3$,and CDI_3," J. Chem. Phys. **125**(17), 174503 (2006).
22. J. Zimmermann, K. Gündoğdu, M. E. Cremeens, J. M. Bandaria, G. T. Hwang, M. C. Thielges, C. M. Cheatum, and F. E. Romesberg, "Efforts toward developing probes of protein dynamics: vibrational dephasing and relaxation of carbon-deuterium stretching modes in deuterated leucine," J. Phys. Chem. B **113**(23), 7991–7994 (2009).
23. S. R. G. Naraharisetty, V. M. Kasyanenko, M. C. Thielges, F. E. Romesberg, and I. V. Rubtsov, "C - D modes of deuterated side chain of leucine as structural reporters *via* dual-frequency two-dimensional infrared spectroscopy," J. Phys. Chem. B **113**(14), 4940–4946 (2009).
24. J. Cavanagh, W. J. Fairbrother, N. J. Skelton, A. G. Palmer, and M. Rance, *Protein NMR Spectroscopy*, (Elsevier Science, 2010).
25. R. R. Ernst, G. Bodenhausen, and A. Wokaun, *Principles of Nuclear Magnetic Resonance in One and Two Dimensions*, (Oxford University Press, 1987).
26. B. M. Luther, K. M. Tracy, M. Gerrity, S. Brown, and A. T. Krummel, "2D IR spectroscopy at 100 KHz utilizing a mid-IR OPCPA laser source," Opt. Express **24**(4), 4117–4127 (2016).
27. P. M. Donaldson, G. M. Greetham, D. J. Shaw, A. W. Parker, and M. Towrie, "A 100 kHz pulse shaping 2D-IR spectrometer based on dual Yb:KGW amplifiers," J. Phys. Chem. A **122**(3), 780–787 (2018).
28. G. M. Greetham, P. M. Donaldson, C. Nation, I. V. Sazanovich, I. P. Clark, D. J. Shaw, A. W. Parker, and M. Towrie, "A 100 kHz time-resolved multiple-probe femtosecond to second infrared absorption spectrometer," Appl. Spectrosc. **70**(4), 645–653 (2016).
29. O.D. Mücke, S. Ališauskas, A. J. Verhoef, A. Pugžlys, A. Baltuška, V. Smilgevičius, J. Pocius, L. Giniūnas, R. Danielius, and N. Forget, "Toward TW-peak-power single-cycle IR fields for attosecond physics and high-field science," In *Advances in Solid State Lasers Development and Applications*, (2010), pp. 279–300.
30. D. R. Skoff, J. E. Laaser, S. S. Mukherjee, C. T. Middleton, and M. T. Zanni, "Simplified and economical 2D IR spectrometer design using a dual acousto-optic modulator," Chem. Phys. **422**, 8–15 (2013).
31. S. H. Shim and M. T. Zanni, "How to turn tour pump-probe instrument into a multidimensional spectrometer: 2D IR and vis spectroscopies *via* pulse shaping," Phys. Chem. Chem. Phys. **11**(5), 748–761 (2009).
32. S. H. Shim, D. B. Strasfeld, Y. L. Ling, and M. T. Zanni, "Automated 2D IR spectroscopy using mid-IR pulse shaping and application of this technology to the human islet amyloid polypeptide," Proc. Natl. Acad. Sci. **104**(36), 14197–14202 (2007).

Optics EXPRESS

33. S. H. Shim, D. B. Strasfeld, E. C. Fulmer, and M. T. Zanni, "Femtosecond pulse shaping directly in the Mid-IR using acousto-optic modulation," Opt. Lett. **31**(6), 838–840 (2006).
34. C. T. Middleton, A. M. Woys, S. S. Mukherjee, and M. T. Zanni, "Residue-specific structural kinetics of proteins through the union of isotope labeling, mid-IR pulse shaping, and coherent 2D IR spectroscopy," Methods **52**(1), 12–22 (2010).
35. A. Ghosh, A. L. Serrano, T. A. Oudenhoven, J. S. Ostrander, E. C. Eklund, A. F. Blair, and M. T. Zanni, "Experimental implementations of 2D IR spectroscopy through a horizontal pulse shaper design and a focal plane array detector," Opt. Lett. **41**(3), 524–527 (2016).
36. P. Hamm and M. Zanni, *Concepts and Methods of 2D Infrared Spectroscopy*, (Cambridge University Press, 2011).
37. M. F. DeCamp and A. Tokmakoff, "Upconversion multichannel infrared spectrometer," Opt. Lett. **30**(14), 1818–1820 (2005).
38. M. J. Nee, R. McCanne, K. J. Kubarych, and M. Joffre, "Two-dimensional infrared spectroscopy detected by chirped pulse upconversion," Opt. Lett. **32**(6), 713–715 (2007).
39. J. M. Nite, J. D. Cyran, and A. T. Krummel, "Active bragg angle compensation for shaping ultrafast mid-infrared pulses," Opt. Express **20**(21), 23912–23920 (2012).
40. M. C. Abrams, G. C. Toon, and R. A. Schindler, "Practical example of the correction of fourier-transform spectra for detector nonlinearity," Appl. Opt. **33**(27), 6307–6314 (1994).
41. R. L. Richardson, H. Yang, and P. R. Griffiths, "Effects of detector nonlinearity on spectra measured on three commercial FT-IR spectrometers," Appl. Spectrosc. **52**(4), 572–578 (1998).
42. D. B. Chase, "Nonlinear detector response in FT-IR," Appl. Spectrosc. **38**(4), 491–494 (1984).
43. F. Bartoli, R. Allen, L. Esterowitz, and M. Kruer, "Auger-limited carrier lifetimes in HgCdTe at high excess carrier concentrations," J. Appl. Phys. **45**(5), 2150–2154 (1974).
44. N. M. Kearns, R. D. Mehlenbacher, A. C. Jones, and M. T. Zanni, "Broadband 2D electronic spectrometer using white light and pulse shaping: noise and signal evaluation at 1 and 100 kHz," Opt. Express **25**(7), 7869–7883 (2017).
45. Y. Feng, I. Vinogradov, and N. H. Ge, "Optimized noise reduction scheme for heterodyne spectroscopy using array detectors," Opt. Express **27**(15), 20323–20346 (2019).
46. Y. Feng, I. Vinogradov, and N. H. Ge, "General noise suppression scheme with reference detection in heterodyne nonlinear spectroscopy," Opt. Express **25**(21), 26262–26279 (2017).
47. K. C. Robben and C. M. Cheatum, "Edge-pixel referencing suppresses correlated baseline noise in heterodyned spectroscopies," J. Chem. Phys. **152**(9), 094201 (2020).
48. D. C. Urbanek, D. Y. Vorobyev, A. L. Serrano, F. Gai, and R. M. Hochstrasser, "The two-dimensional vibrational echo of a nitrile probe of the villin HP35 protein," J. Phys. Chem. Lett. **1**(23), 3311–3315 (2010).
49. P. Marek, S. Mukherjee, M. T. Zanni, and D. P. Raleigh, "Residue-specific, real-time characterization of lag-phase species and fibril growth during amyloid formation: a combined fluorescence and IR study of p-cyanophenylalanine analogs of islet amyloid polypeptide," J. Mol. Biol. **400**(4), 878–888 (2010).
50. R. E. Horness, E. J. Basom, and M. C. Thielges, "Site-selective characterization of the src homology 3 domain molecular recognition with cyanophenylalanine infrared probes," Anal. Methods **7**(17), 7234–7241 (2015).
51. A. L. Le Sueur, S. Ramos, J. D. Ellefsen, S. Cook, and M. C. Thielges, "Evaluation of P-(^{13}C,^{15}N-cyano)phenylalanine as an extended time scale 2D IR probe of proteins," Anal. Chem. **89**(10), 5254–5260 (2017).
52. S. Bagchi, S. G. Boxer, and M. D. Fayer, "Ribonuclease S dynamics measured using a nitrile label with 2D IR vibrational echo spectroscopy," J. Phys. Chem. B **116**(13), 4034–4042 (2012).
53. D. V. Kurochkin, S. R. G. Naraharisetty, and I. V. Rubtsov, "Dual-frequency 2D IR on interaction of weak and strong IR modes," J. Phys. Chem. A **109**(48), 10799–10802 (2005).
54. D. E. Rosenfield, Z. Gengeliczki, B. J. Smith, T. D. P. Stack, and M. D. Fayer, "Structural dynamics of a catalytic monolayer probed by ultrafast 2D IR vibrational echoes," Science **334**(6056), 634–639 (2011).
55. T. A. Oudenhoven, "Advances in 2D IR spectroscopy and applications to sensitized thin films," Ph.D Dissertation, (University of Wisconsin-Madison, Madison, WI, 2015).
56. S. Woutersen and P. Hamm, "Nonlinear two-dimensional vibrational spectroscopy of peptides," J. Phys.: Condens. Matter **14**(39), R1035–R1062 (2002).
57. L. Ackels, P. Stawski, K. E. Amunson, and J. Kubelka, "On the temperature dependence of amide I intensities of peptides in solution," Vib. Spectrosc. **50**(1), 2–9 (2009).
58. J. Kubelka and T. A. Keiderling, "Ab initio calculation of amide carbonyl stretch vibrational frequencies in solution with modified basis sets. 1. *N*-Methyl Acetamide," J. Phys. Chem. A **105**(48), 10922–10928 (2001).
59. M. Grechko and M. T. Zanni, "Quantification of transition dipole strengths using 1D and 2D spectroscopy for the identification of molecular structures *via* exciton delocalization: application to α-helices," J. Chem. Phys. **137**(18), 184202 (2012).
60. J. P. Lomont, J. S. Ostrander, J. J. Ho, M. K. Petti, and M. T. Zanni, "Not all β-sheets are the same: amyloid infrared spectra, transition dipole strengths, and couplings investigated by 2D IR spectroscopy," J. Phys. Chem. B **121**(38), 8935–8945 (2017).
61. E. B. Dunkelberger, M. Grechko, and M. T. Zanni, "Transition dipoles from 1D and 2D infrared spectroscopy help reveal the secondary structures of proteins: application to amyloids," J. Phys. Chem. B **119**(44), 14065–14075 (2015).

Optics EXPRESS

62. K. M. Tracy, M. V. Barich, C. L. Carver, B. M. Luther, and A. T. Krummel, "High-throughput two-dimensional infrared (2D IR) spectroscopy achieved by interfacing microfluidic technology with a high repetition rate 2D IR spectrometer," J. Phys. Chem. Lett. **7**(23), 4865–4870 (2016).
63. S. S. Mukherjee, D. R. Skoff, C. T. Middleton, and M. T. Zanni, "Fully absorptive 3D IR spectroscopy using a dual mid-infrared pulse shaper," J. Chem. Phys. **139**(14), 144205 (2013).
64. R. Schanz, V. Boţan, and P. Hamm, "A femtosecond study of the infrared-driven cis-trans isomerization of nitrous acid (HONO)," J. Chem. Phys. **122**(4), 044509 (2005).
65. J. Crank, *The Mathematics of Diffusion*, (Oxford Science Publications, 1975), pp. 241–244.